



# Numerical simulation of the atmospheric boundary layer over laboratory-scale two-dimensional hill using pressure-driven boundary condition

R. Lakshman\*, B. Ranjan

*National Institute of Technology Sikkim, Ravangla, Sikkim, India*

## Abstract

The atmospheric boundary layer (ABL) is the lowest part of the atmosphere directly impacted by the earth's surface. ABL simulation is essential for predicting wind load, pollutant dispersion, and wind capacity over a terrain. ABL can be modeled using the computational fluid dynamics (CFD) tool. Maintaining horizontal homogeneity is critical for a more accurate ABL simulation. Researchers have proposed various boundary conditions for obtaining homogeneously homogeneous ABL. This study investigates pressure-driven boundary conditions for the atmospheric boundary layer over a laboratory-scale two-dimensional (2D) hill. For complex terrains, such as a 2D hill, the numerical analysis of pressure-driven flow has not yet been considered. The validation was done using the experimental results from the ERCOFTAC 69 case, namely a simplified 2D hill. The results are also compared with the shear-driven boundary conditions. The results of simulations of ABL employing pressure-driven boundary conditions using different turbulence models have also been compiled. From MAPE analysis, it is found that the results of ABL simulation using pressure-driven boundary conditions produced lower MAPE values, resulting in superior outcomes compared to the shear-driven boundary conditions.

**Keywords:** Turbulence modeling, OpenFOAM, Atmospheric boundary layer, RANS, boundary conditions

## 1. Introduction

The lowest portion of the troposphere immediately affected by the presence of the earth's surface is known as the atmospheric boundary layer (ABL). The surface of the earth directly influences the behavior of ABL. Simulation of ABL is very much required for various studies like assessing wind load [1], estimating pollution dispersion, calculating wind load over a particular terrain, etc. ABL simulation is generally carried out experimentally inside a wind tunnel test section or numerically using computational fluid dynamic (CFD) tools. The wind tunnels which is used for ABL simulation are called atmospheric boundary layer wind tunnels. Since it requires a very long test section, the experimental simulation requires a very big space for installation. As a result, it takes a lot of time and is not very economical. Numerical studies of atmospheric flows have received much attention since computers have been utilized to handle complicated numerical problems [2-6]. The effects of boundary layers on various surfaces are of considerable interest to many researchers [7], and the interest in ABL is also evident. CFD analysis of ABL helps to study the spread of pollutants, risk assessment, optimal placing of wind farm sites, and microclimate studies. Recent years have seen a lot of effort focused on the development of novel structures, technologies, systems, and energies [8-40].

---

\* Corresponding author. Tel.: +918089276705  
E-mail address: lakshmanr03@gmail.com

The turbulence models, large-eddy simulations (LES), or Reynolds-averaged Navier-Stokes (RANS) equations can be used to simulate ABL flows numerically. Since the LES simulation is costly and time-consuming, realistic ABL flows modeling is still widely solved using RANS equations [41, 42]. The influences of roughness on ABL flows are commonly modeled in RANS simulations using wall functions based on sand grain height [43], which relies on flow measurements conducted in rough, circular pipes covered with sand [44]. The impact of buoyancy [45, 46] and the Coriolis force can be disregarded when simulating ABL close to the surface. Neutral ABL simulation can be used to represent simulation that takes place close to the surface.

A neutral ABL is referred to as horizontally homogeneous (HHABL) if there is no streamwise variation in fluid flow properties. The HHABL flows are widely simulated using the velocity, turbulence dissipation rate, and turbulence kinetic energy profiles proposed by Richards and Hoxey [47]. In HHABL flows, the profiles of the parameters must be the same at the inlet and outlet. However, because Richards and Hoxey propose a constant value inlet profile for turbulence kinetic energy ( $k$ ), in contrast to wind-tunnel results, this modeling technique may result in a poor replication of the ABL. Another inconsistency found in the profile suggested by Richards and Hoxey is the conflict between the fully developed ABL inlet profile and rough wall functions [48-50]. These concerns were resolved by Yang et al. [51], who introduced a new set of inflow conditions in which the turbulence kinetic energy profile is a function of the domain height. Both of these inflow conditions are shear-driven boundary conditions. The top wall of the domain will be supplied with constant shear stress in both cases. Many other researchers also come up with inflow conditions consistent with the turbulence model [52-54]. Richards and Norris derived the boundary conditions for an equilibrium pressure-driven flow using all RANS turbulence models [55]. Several recommendations have been provided by Richards and Norris related to the choice and implementation of experimental data as boundary conditions for the simulation of ABL[56].

In this paper, the numerical study of ABL flow employing pressure-driven and shear-driven boundary conditions has been conducted over a laboratory-scale two-dimensional hill. The boundary conditions proposed by Richards and Hoxey, Yang et al., and Richards and Norris were used for the analysis. For complex terrains, such as a 2D hill, the numerical analysis of pressure-driven flow has not yet been considered. Hence, this study is highly innovative, which inspired us to undertake this analysis. Furthermore, there hasn't yet been a comparative analysis of boundary conditions for pressure-driven and shear-driven boundary layers for any terrain. The numerical analysis has been carried out using the open-source CFD tool OpenFOAM [57]. Many researchers have recently expressed an interest in working with OpenFOAM [58-60]. A comparative study of different RANS turbulence models was also carried out using the boundary condition suggested by Richards and Norris.

## 2. Background

The horizontal homogeneity of the ABL profile throughout the computational domain is one of the key parameters affecting the consistency of CFD simulations of ABL [61]. The inflow conditions have a great role in maintaining horizontal homogeneity. The boundary conditions employed in this paper are discussed in the following subsections

### 2.1. Inlet profiles proposed by Richards and Hoxey (1993)

Richards and Hoxey (1993) developed one of the most often used inflow boundary conditions for neutral ABL. Based on the logarithmic law profile, they presented the inflow boundary conditions for mean velocity ( $U$ ), turbulence kinetic energy ( $k_{RH}$ ), and turbulence dissipation rate ( $\epsilon$ ), as indicated by Eqs. (1)–(3) respectively

$$U = \frac{u_\tau}{\kappa} \ln \left( \frac{z + z_0}{z_0} \right) \quad (1)$$

$$k_{RH} = \frac{u_\tau^2}{\sqrt{c_\mu}} \quad (2)$$

$$\epsilon = \frac{u_\tau^3}{\kappa(z + z_0)} \tag{3}$$

The above-mentioned inflow boundary conditions will satisfy the model only if the turbulent Prandtl number,  $\sigma_\epsilon$  of the dissipation rate is represented as Eq. (4).

$$\sigma_\epsilon = \frac{\kappa^2}{(C_{\epsilon 2} - C_{\epsilon 1})C_\mu^{0.5}} \tag{4}$$

where,  $U$ ,  $\epsilon$ ,  $k$  are the inlet mean velocity, turbulence dissipation rate, and turbulence kinetic energy, respectively;  $\kappa$  is the Von Karman constant,  $u_\tau$  is the frictional velocity,  $z_0$  is the aerodynamic roughness length,  $C_{\epsilon 1}$ ,  $C_{\epsilon 2}$  and  $c_\mu$  are the turbulence model parameters.

2.2. Inlet profiles proposed by Yang et al. (2009)

Yang et al. [2009] proposed a more realistic boundary condition for turbulent kinetic energy Eq. (5). In contrast to Richards and Hoxey's constant turbulence kinetic energy profile, the profile suggested by Yangs et al. varies with height, which is compatible with experimental observations. Apart from the new turbulence kinetic energy profile, Yang et al. used the same profile for the mean velocity profile and turbulence dissipation rate given in Eq. (1) and Eq.(3), respectively.

$$k_{YANG} = \sqrt{C_{y1} \ln(z + z_0) + C_{y2}} \tag{5}$$

where,  $C_{y1}$  and  $C_{y2}$  are model constants obtained from fitting the profile to the experimental data.

2.3. Inlet profiles proposed by Richards and Norris (2015)

According to Richard and Norris (2015), the atmospheric flow is primarily controlled by pressure drop when there is no definite shear stress at the domain's top, which might result in significant streamwise non - uniformity. Streamwise homogeneity for the mean velocity and turbulent quantities are ensured by Richards and Norris's inlet profiles for the stable pressure-driven boundary layer, including the decaying of turbulent kinetic energy with domain height. They have proposed the profiles for both  $k - \epsilon$  and  $k - \omega$  turbulence models. The expressions for the mean velocity profile ( $U_{RN}$ ), turbulence kinetic energy profile ( $k_{RN}$ ), and turbulence dissipation rate ( $\epsilon_{RN}$ ) proposed by Richards and Norris are shown in Eqs. (6)-(8).

$$U_{RN} = \frac{U_\tau}{\kappa} \left( \ln\left(\frac{z}{z_0}\right) + C_{u1} \left(\frac{z}{H}\right) + C_{u2} \left(\frac{z}{H}\right)^2 + C_{u3} \left(\frac{z}{H}\right)^3 + C_{u4} \left(\frac{z}{H}\right)^4 \right) \tag{6}$$

$$k_{RN} = U_\tau^2 \left( C_{k1} + C_{k2} \left(1 - \frac{z}{H}\right)^2 + C_{k3} \left(1 - \frac{z}{H}\right)^4 + C_{k4} \left(1 - \frac{z}{H}\right)^6 \right) \tag{7}$$

$$\epsilon_{RN} = \frac{C_\mu k_{(z)}^2}{\kappa U_\tau z} \left( 1 + (1 + C_{U1}) \left(\frac{z}{H}\right) + (1 + C_{U1} + 2C_{u2}) \left(\frac{z}{H}\right)^2 + (1 + C_{U1} + 2C_{u2} + 3C_{u3}) \left(\frac{z}{H}\right)^3 \right) \tag{8}$$

where  $C_{u1}$ ,  $C_{u2}$ ,  $C_{u3}$  and  $C_{u4}$  are the polynomial coefficients used to calculate velocity, and their values for the  $k-\epsilon$  turbulence model are 0.528, 0.385, -1.090, and 0.243, respectively.  $C_{k1}$ ,  $C_{k2}$ ,  $C_{k3}$  and  $C_{k4}$  are the polynomial constants used for calculating turbulence kinetic energy, whose values are 0.921, 3.533, -1.926, and 0.805, respectively.

### 3. Numerical Modelling

All OpenFOAM simulations in this analysis were performed with the SimpleFoam solver, a steady-state, incompressible solver. The Gaussian integration was employed with various interpolation strategies for the spatial discretization of differential operators. 2nd order upwind interpolation for divergence terms, 2nd order linear interpolation for gradient terms, and 2nd order linear interpolation with explicit non-orthogonal correction for Laplacian terms was used. For pressure, the preconditioned conjugate gradient solver was used with a simplified diagonal-based incomplete Cholesky preconditioner, while for velocity and turbulence, its bi-conjugate variant was used with an incomplete LU preconditioner. For pressure-velocity coupling, the SIMPLE technique was utilized. The relaxation parameters were set to 0.3 for pressure and 0.7 for the other prognostic variables as a default. A convergence tolerance of  $10^{-8}$  is given for all the parameters

#### 3.1. Domain details

The model problem used was the same as that given by ERCOFTAC 69 case [62], namely a simplified 2D hill.

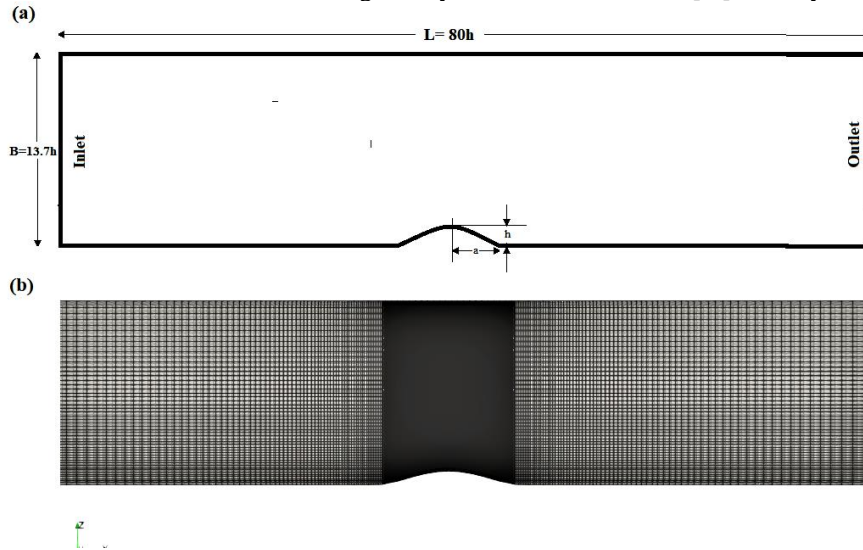


Figure 1: (a) Domain details of the 2D hill; (b) mesh details of the domain

The schematic of the domain and the mesh details are shown in Figure. 1. The computational domain (Figure.1 (a)) is symmetrical to the hill axis, and it measures  $80h \times 13.7h$  (where 'h' is the height of the hill). The height of the hill (h) has been taken as 0.117m corresponds to ERCOFTAC 69 case. Three different types of hills are taken for the analysis based on the hill's aspect ratio (a/h). The hill with aspect ratios 3, 5, and 8 are named 3H Hill, 5H Hill, and 8H Hill, respectively. The shape of the hills was obtained using Eq. (9) and Eq. (10).

$$y(\zeta) = 0.5m \sqrt{(a^2 - \zeta^2)} \left[ 1 - \left( \frac{a^2}{\zeta^2 + m^2(a^2 - \zeta^2)} \right) \right] \quad (9)$$

$$x(\zeta) = 0.5\zeta \left[ 1 + \left( \frac{a^2}{\zeta^2 + m^2(a^2 - \zeta^2)} \right) \right] \quad (10)$$

where  $m = n + \sqrt{n^2 + 1}$  is the shape parameter and  $n = \frac{h}{a}$  is the average slope. Block structured meshes are prepared by applying four different mesh resolutions using  $(460 * 50)$ ,  $(350 * 50)$ ,  $(170 * 50)$ , and  $(85 * 50)$  cells.

The grid independence study is also conducted using the four grids mentioned above.

**Table 1: Values of parameters used for simulating different hills**

Type of hill	$U_\tau$ (m/s)	$z_0$
3H	0.2053	0.0004972
5H	0.1988	0.0003576
8H	0.1829	0.0001586

### 3.2. Boundary Condition

The inlet boundary conditions are based on the RH, YANG, and RN model's boundary conditions. Shear-driven boundary conditions are provided by the RH and YANG models, while pressure-driven boundary conditions are provided by the RN model. In the first two cases, the top wall has fixed shear stress, while the top wall has a no-slip boundary condition in the third case. Table 1 shows aerodynamic roughness length ( $z_0$ ) and friction velocity  $U_\tau$  for various hills.

### 3.3. Grid Independence study

A grid-independent analysis was performed with four different types of grids (Type I, Type II, Type III, and Type IV) and are investigated and analyzed using RN inlet conditions. Table 2 lists the mesh arrangements in detail. Type I has a very coarse mesh, while Type IV has the finest mesh in the table

**Table 1: Details of the meshes used for the grid independence study**

Type of Mesh	Grid Arrangement	Total number of cells
Type I	85 * 50	3400
Type II	170 * 50	8500
Type III	350 * 50	16000
Type IV	460 * 50	23000

Figure 2 shows numerical results of the simulation on all four meshes are quite close. Figure. 2 shows the results closer to the surface, where the derivations are more visible. As seen from the Figure, the results of Type I and Type II are inferior to Type III and Type IV, which have finer mesh configurations. When using Type III and Type IV configurations, the results obtained only very little difference. As a result, the Type III mesh arrangement was chosen for all the cases to reduce calculation time and speed up the computation.

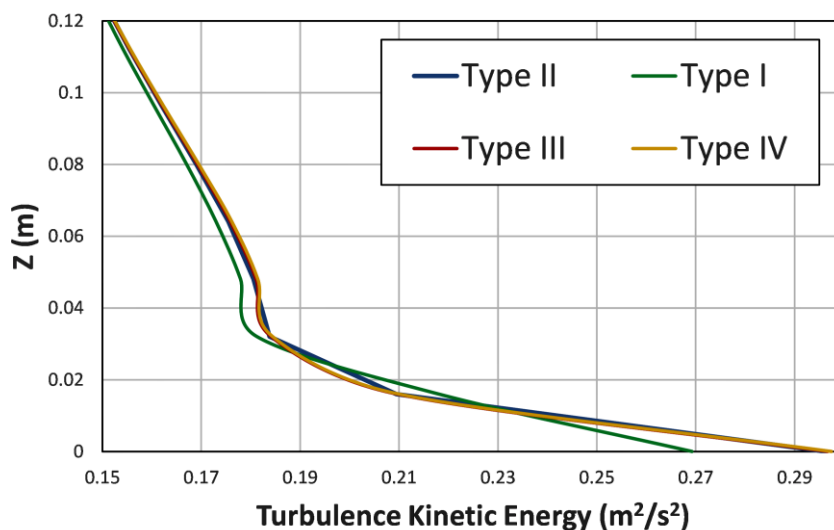


**Figure 2: Turbulence kinetic energy profile for various grids used for grid independence near the surface**

## 4. Results and Discussion

### 4.1. Comparative analysis of boundary conditions for pressure-driven and shear-driven boundary layers

The mean velocity profile obtained above the hill summit using various inlet boundary conditions for hills with different aspect ratios is shown in Figure 3. Although the outcomes of velocity for the 3H Hill do not match precisely with the experimental data in the case of the RH and YANG models, the RN model delivers excellent results. In the case of the RH model, the results differ slightly from the experimental value towards the top and significantly near the hill summit. The YANG model produced similar results, but the deviation towards the top of the hill is more pronounced. Similar findings are found in the case of 5H Hills, with the RN model outperforming the other models. However, when it comes to 5H Hill, the deviation from the experimental data for RH and YANG models is slightly lower than when it comes to 3H Hill. When compared to the results from hills with a low aspect ratio, the results for 8H are vastly improved for all models. In the instance of 8H Hill, the results are getting closer to the experimental value for all models. Based on the findings, it can be concluded that better simulation results are obtained when the aspect ratio increases.

Figure 4(a) shows the turbulent kinetic energy profile obtained by using different types of inlet boundary conditions in the case of 3H Hill. Figure 4(a) shows that the turbulent kinetic energy obtained at the hill's summit using the RH inlet condition differs significantly from the experimental data. When the distance from the hill is greater than 0.1 m, a significant difference can be seen.

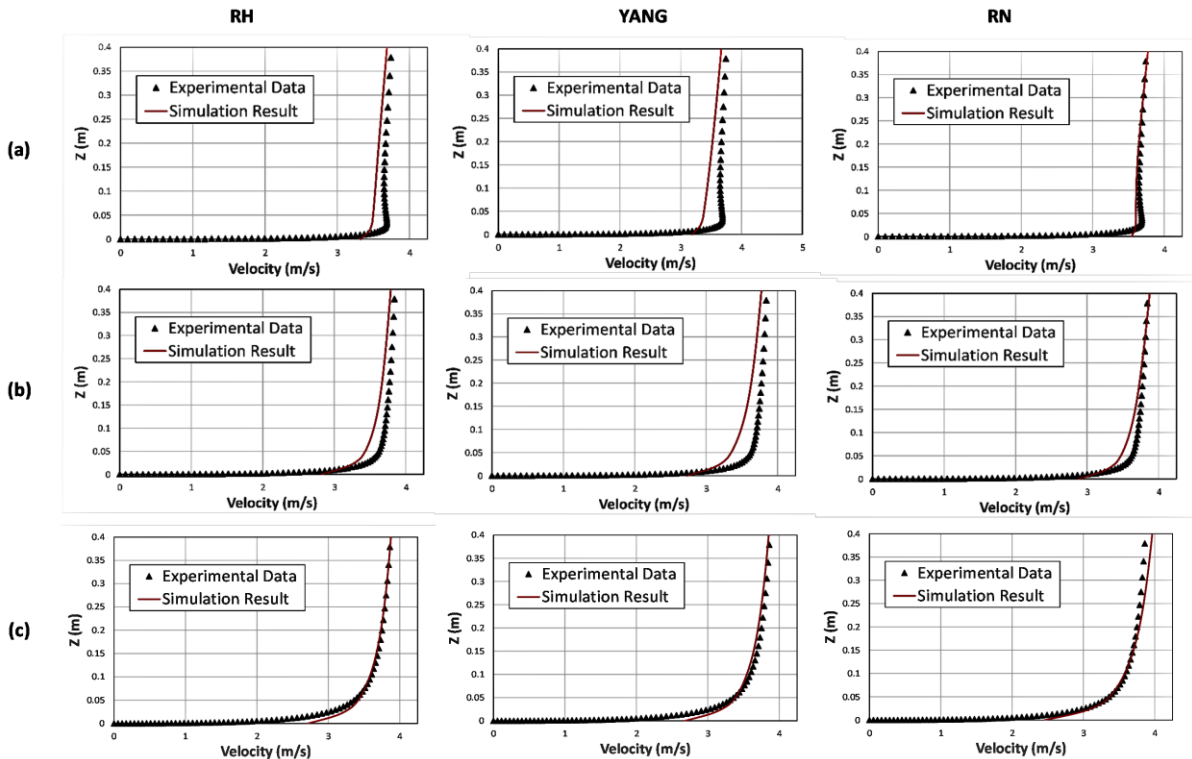
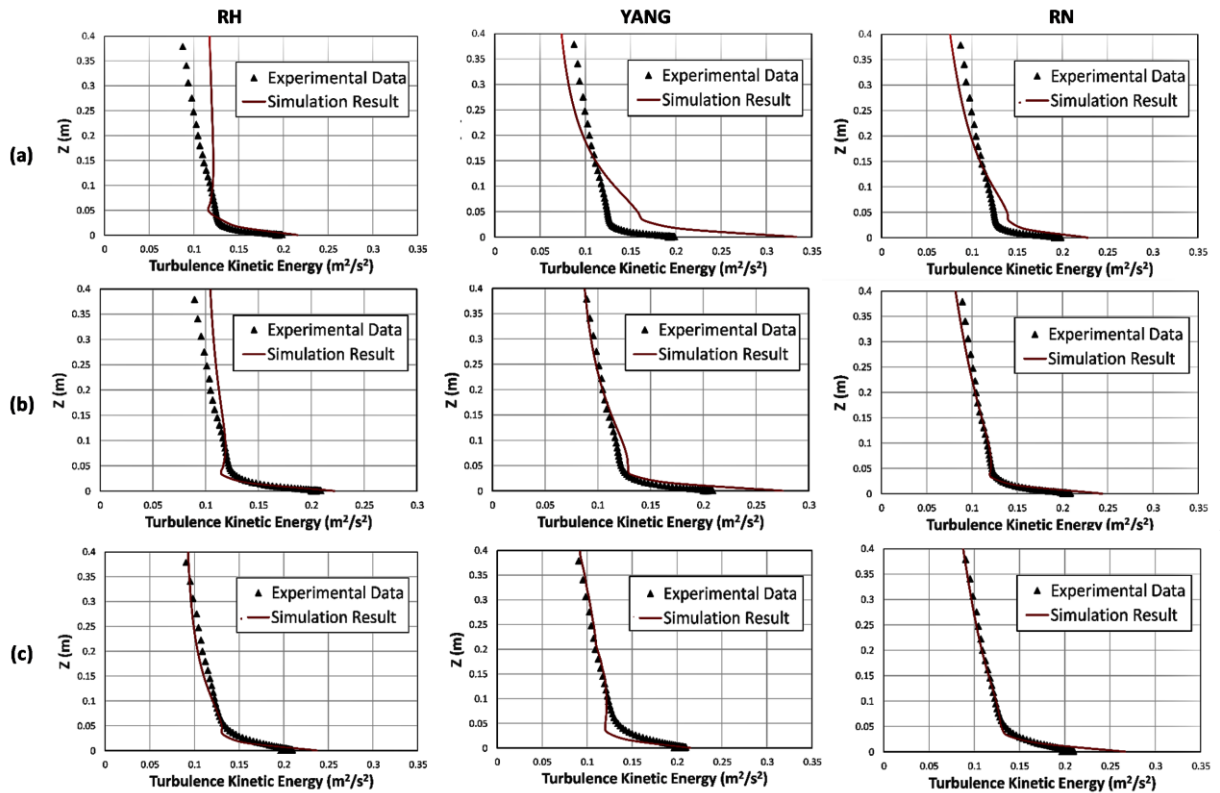


Figure 3: Mean velocity profile above the hill summit using RH model, YANG model, and RN model for (a) 3H Hill, (b) 5H Hill, (c) 8H Hill



**Figure 4:** Turbulence kinetic energy profile above the hill summit using RH model, YANG model, and RN model for (a) 3H Hill; (b) 5H Hill; (c) 8H Hill

Using the YANG inlet condition, we can see that the experimental and simulation data differ even more, with the simulation data crossing over the experimental data at the height of 0.15m above the surface. It can also be noticed in the Figure that the profiles become highly different as you get closer to the surface. The experimental and simulation results of turbulence kinetic energy profiles get near when we use the RN profile. As seen in the Figure, the value of simulation results approaches the experimental data at the top and at the surface. While considering all of the results from 3H Hill, It can be seen that the simulation results are not particularly near the experimental value. Still, as compared to other models, the results produced using RN inlet conditions are closer to experimental.

Although the results from 5H Hill employing the RH inlet condition are superior to those from 3H Hill, there is some variation as we go above the hills from around 0.1m (Figure 4. (b) RH). Compared to 3H Hill, the results obtained using the YANG inlet conditions were substantially more satisfactory. Compared to the results obtained in 3H Hill, the YANG model significantly improves both close and far from the surface. In the case of the RN model, the generated results are quite similar to the experimental data

In the context of 8H Hill, all of the models show encouraging results. The simulation results and experimental data in Figure 4 (c) are pretty close for all models. Regarding 8H Hills, the RH model shows significant improvement (Figure4. (c) RH). The YANG model produces excellent results compared to other hills with a lower aspect ratio (Figure4. (c) YANG). The RN model outperforms the others in simulation outcomes, and its prediction is practically identical to the experimental data. As shown in the Figure, the simulation results in all models improve dramatically whenever the aspect ratio is increased. However, the RN model produces better outcomes even when the aspect ratio is low compared to others.

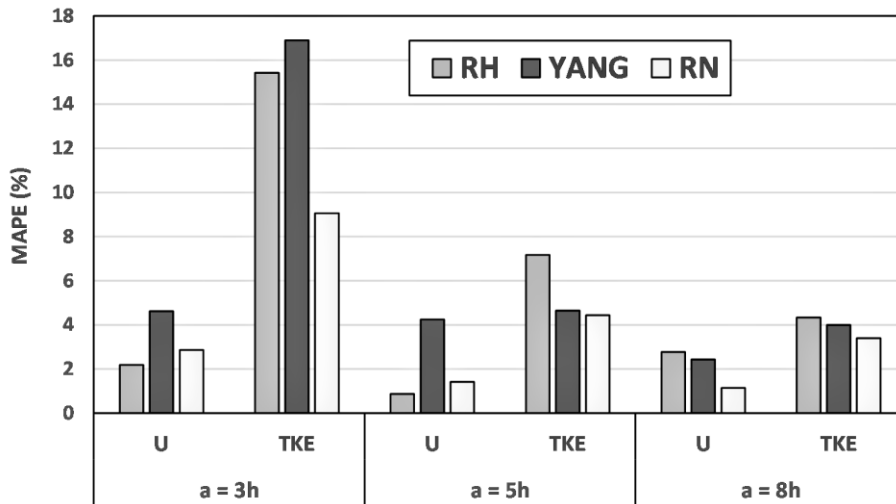


Figure 5: MAPE analysis of mean velocity and turbulence kinetic energy for various models

The Mean Absolute Percentage Error (MAPE), or simply the percentage difference between two data sets, has been calculated between the inlet and outlet simulation data. The MAPE values for mean velocity (U), turbulence kinetic energy (k), and turbulence dissipation rate ( $\epsilon$ ) for different models are shown in Figure 5. MAPE value is estimated using Eq. (11).

$$MAPE = \frac{1}{n} \sum \left| \frac{A_i - A_o}{A_i} \right| \times 100 \tag{11}$$

where,  $A_i, A_o$  are the experimental and simulation value for various parameters (velocity, turbulence kinetic energy, and turbulence dissipation rate)

Compared to other hills, Hills with an aspect ratio of 3 have a comparatively high MAPE value, as shown in Figure 5. The MAPE value is very high for turbulent kinetic energy when compared to velocity. The MAPE value for turbulent kinetic energy steadily reduces as the aspect ratio of the hill increases when results are obtained using RH inlet conditions. YANG model produces outcomes that are comparable to those of the RH model. When it comes to the YANG model, velocity has similar results to those of turbulent kinetic energy. It is seen from the results that the higher the hill's aspect ratio, the lower the MAPE value. Figure 5 shows that the RN model results have the lowest MAPE value of all the models in both turbulent kinetic energy and velocity cases. As the aspect ratio of the hill increases, the MAPE value gradually decreases, similar to other models. From Figure.5, it is evident that the results produced using the RN model outperform the results obtained using other models in both the turbulent kinetic energy and velocity cases.

Table 3: Values of polynomial coefficients for RN model

Turbulence model	$C_{k1}$	$C_{k2}$	$C_{k3}$	$C_{k3}$	$C_{U1}$	$C_{U2}$	$C_{U3}$	$C_{U4}$
$k - \epsilon$	0.921	3.533	-1.926	0.805	0.528	0.385	-1.090	0.243
SST $k - \omega$	1.056	2.814	-0.834	0.297	0.280	-0.331	-0.334	0.096
$k - \omega$	0.810	4.046	-2.623	1.100	0.333	-0.666	0.465	-0.349

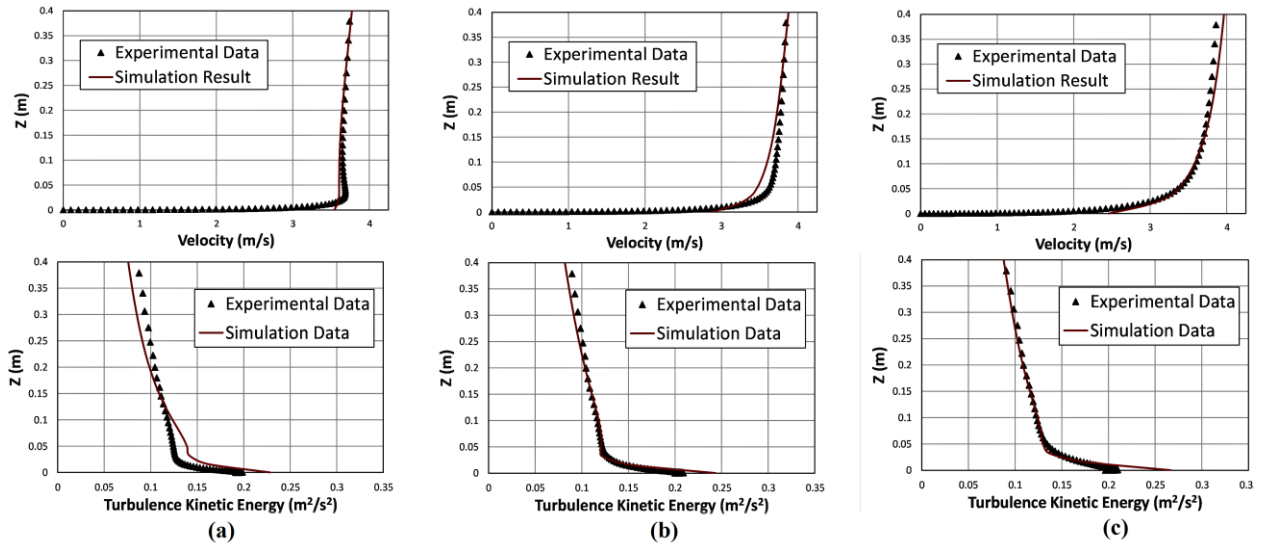


Figure 6: Mean velocity profile and turbulence kinetic energy profile above the hill summit using  $k - \epsilon$  turbulence model with RN model for (a) 3H Hill, (b) 5H Hill, (c) 8H Hill

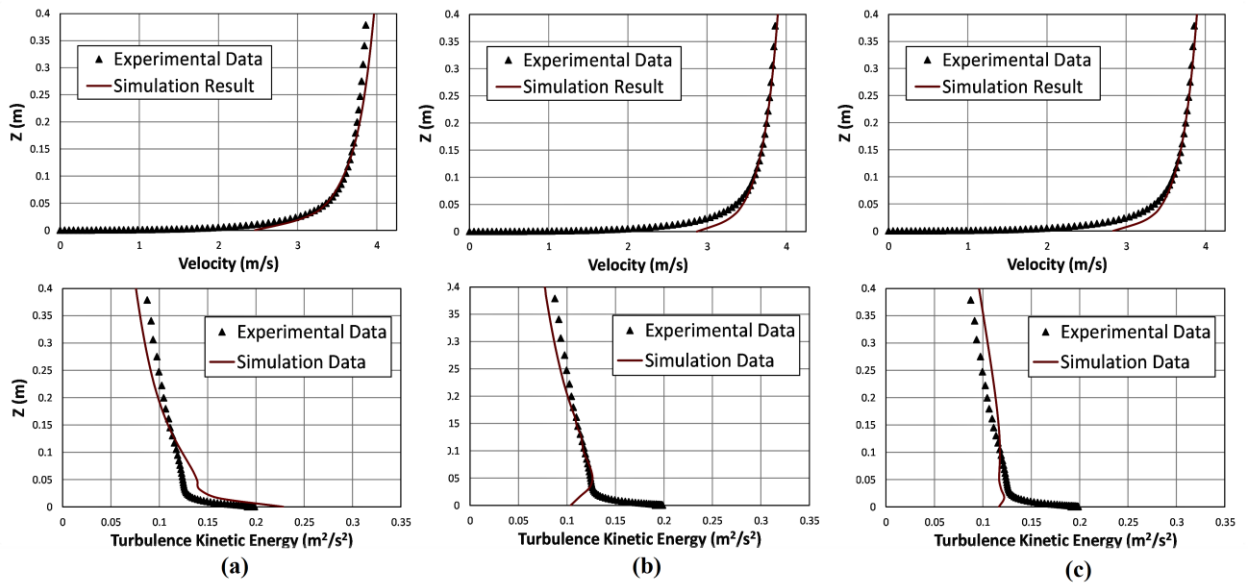
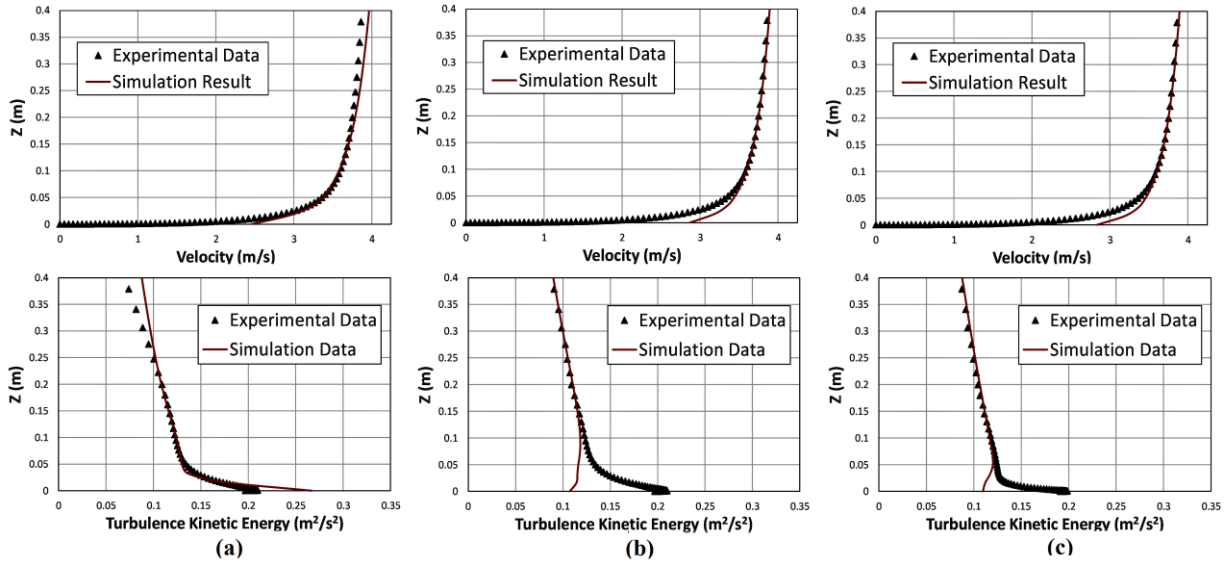


Figure 7: Mean velocity profile and turbulence kinetic energy profile above the hill summit using  $k - \omega$  turbulence model with RN model for (a) 3H Hill, (b) 5H Hill, (c) 8H Hill



**Figure 8: Mean velocity profile and turbulence kinetic energy profile above the hill summit using SST  $k-\omega$  turbulence model with RN model for (a) 3H Hill, (b) 5H Hill, (c) 8H Hill**

#### 4.2. Comparative analysis of turbulence models using boundary conditions for pressure-driven boundary layer

Based on the above observations, the RN model produces superior results for ABL simulation over a 2D hill compared to other models that are taken for the comparative analysis. All three RANS turbulence models ( $k-\epsilon$ ,  $k-\omega$  and SST  $k-\omega$  turbulence models) were used to further analyze the RN model's effectiveness (pressure-driven boundary condition) in simulating ABL flow over a 2D hill. The boundary conditions used are given in Eq (6)-(8). The values of polynomial coefficients for the equations are shown in Table 3. The polynomial coefficients are taken based on the recommendation of Richard and Norris. For each turbulence model, the values of each coefficient are different.

Figure 6 shows the results obtained for 3H Hill using various turbulence models and the RN model as the inlet condition. The  $k-\epsilon$  model provides extremely good results in the case of velocity; however, as seen in Figure 6 (a), the results for turbulent kinetic energy do not match experimental data, both near and far from the hill summit. In both velocity and turbulence kinetic energy, the  $k-\omega$  model results are superior to those obtained using the  $k-\epsilon$  model. Similar results are seen for the SST  $k-\omega$  model. Both the  $k-\omega$  and SST  $k-\omega$  models, in comparison to the  $k-\epsilon$  model, provide excellent results both near and far from the hill summit.

Results for 5 H Hill were obtained using various turbulence models and the RN inlet condition, as shown in Figure.7. Compared to 3H Hill, the turbulence kinetic energy profile produced by the  $k-\epsilon$  model is improving, whereas the  $k-\omega$  model has excellent results away from the hilltop, but it has erroneous results near the hill summit. Similar tendencies can be seen in the SST  $k-\omega$  model.

Figure 8 shows that the results of the turbulence kinetic energy, as well as the velocity profile for the turbulence model, have improved in the case of 8H Hill. The results of  $k-\omega$  model turbulence kinetic energy profile was found to be deteriorating when approaching the hill summit. However, when it comes to outcomes near the summit of the hill, it is likewise inferior to the  $k-\epsilon$  model. Based on the findings, it can be concluded that as the hill's aspect ratio improves, more significant results are achieved. For hills with a low aspect ratio, the  $k-\omega$  turbulence model performs better, whereas the  $k-\epsilon$  turbulence model performs better at the summit.

The MAPE analysis of data acquired using various turbulence models while employing the RN model as the inlet boundary condition is shown in Figure 9. As can be observed in the Figure, as the value of the hill's aspect ratio increases, the value of MAPE decreases, similar to the previous MAPE analysis. Although the results for turbulent kinetic energy are nearly the same for the  $k-\epsilon$  and  $k-\omega$  and SST  $k-\omega$  models, the  $k-\epsilon$  model produces better velocity profile results. Based on the MAPE analysis, it can be concluded that the  $k-\epsilon$  model may be employed for simulation to obtain better results than other models.

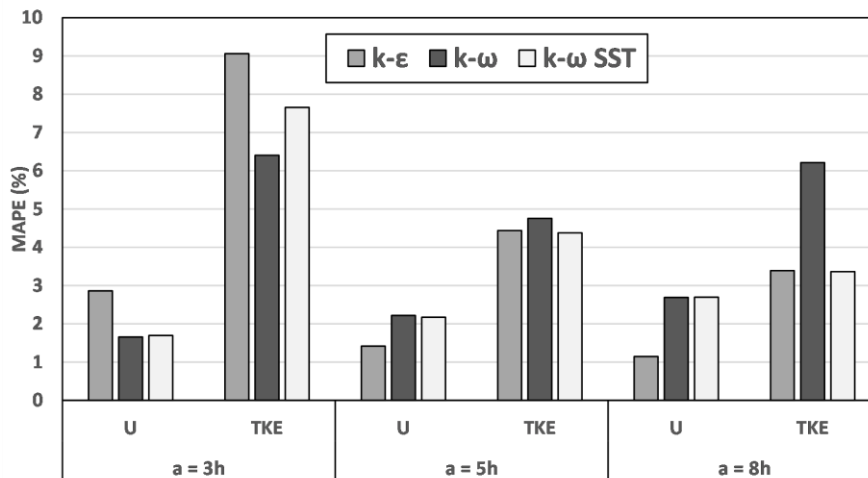


Figure 9: MAPE analysis of mean velocity and turbulence kinetic energy for various turbulence models using with RN model

## 5. Advantages and limitations of pressure-driven boundary conditions

For ABL simulation, pressure-driven boundary conditions have many advantages over shear-driven boundary conditions; notable among them was the ease of implementation and the high level of consistency of the result with experimental data. Although producing better results than other models, ABL simulation based on the pressure-driven boundary condition model is found to be insufficient for separated regions. Additional research can be done using the Building Influence Area (BIA) technique to get around this restriction.

## 6. Conclusion

- ABL Simulation has been done over a laboratory-scale 2D hill using boundary conditions for shear-driven (RH and YANG models) and pressure-driven (RN model) boundary layers
- The results revealed that the simulation over hills with a higher aspect ratio produces better results.
- It was observed that RN boundary conditions perform better than the other two boundary conditions for the flow over a two-dimensional hill.
- A MAPE analysis was also performed for result analysis, and the RN model simulation produced lower MAPE values, resulting in superior results.
- The analysis shows that superior results are obtained while employing the SST  $k - \omega$  turbulence model with the RN model compared to other turbulence models.
- Despite producing better results than other models, the RN model is found to be inadequate for separated regions. Further analysis can be done by incorporating Building Influence Area (BIA) technique to mitigate this limitation.

## Acknowledgment

The authors would like to extend their sincere gratitude to the reviewers for their valuable recommendations.

## References

- [1] S. E. Hosseindoost, A. Sattari, M. Eskandari, D. Vahidi, P. Hanafizadeh, P. Ahmadi, Techno-economy study of wind energy in Khvaf in Razavi Khorasan Province in Iran, *Journal of Computational Applied Mechanics*, Vol. 47, No. 1, pp. 53-66, 2016.
- [2] F. Mebarek-Oudina, Numerical modeling of the hydrodynamic stability in vertical annulus with heat source of different lengths, *Engineering science and technology, an international journal*, Vol. 20, No. 4, pp. 1324-1333, 2017.
- [3] V. N. Mishra, *Some problems on approximations of functions in Banach spaces*, Thesis, Ph. D. thesis, 2007.

- [4] M. Farhan, Z. Omar, F. Mebarek-Oudina, J. Raza, Z. Shah, R. Choudhari, O. Makinde, Implementation of the one-step one-hybrid block method on the nonlinear equation of a circular sector oscillator, *Computational Mathematics and Modeling*, Vol. 31, No. 1, pp. 116-132, 2020.
- [5] I. Chabani, F. Mebarek-Oudina, A. A. I. Ismail, MHD Flow of a Hybrid Nano-fluid in a Triangular Enclosure with Zigzags and an Elliptic Obstacle, *Micromachines*, Vol. 13, No. 2, pp. 224, 2022.
- [6] L. N. Mishra, M. Sen, R. N. Mohapatra, On existence theorems for some generalized nonlinear functional-integral equations with applications, *Filomat*, Vol. 31, No. 7, pp. 2081-2091, 2017.
- [7] R. Djebali, F. Mebarek-Oudina, C. Rajashekhar, Similarity solution analysis of dynamic and thermal boundary layers: Further formulation along a vertical flat plate, *Physica Scripta*, Vol. 96, No. 8, pp. 085206, 2021.
- [8] H. Asemi, S. Asemi, A. Farajpour, M. Mohammadi, Nanoscale mass detection based on vibrating piezoelectric ultrathin films under thermo-electro-mechanical loads, *Physica E: Low-dimensional Systems and Nanostructures*, Vol. 68, pp. 112-122, 2015.
- [9] S. Asemi, A. Farajpour, H. Asemi, M. Mohammadi, Influence of initial stress on the vibration of double-piezoelectric-nanoplate systems with various boundary conditions using DQM, *Physica E: Low-dimensional Systems and Nanostructures*, Vol. 63, pp. 169-179, 2014.
- [10] S. Asemi, A. Farajpour, M. Mohammadi, Nonlinear vibration analysis of piezoelectric nanoelectromechanical resonators based on nonlocal elasticity theory, *Composite Structures*, Vol. 116, pp. 703-712, 2014.
- [11] S. R. Asemi, M. Mohammadi, A. Farajpour, A study on the nonlinear stability of orthotropic single-layered graphene sheet based on nonlocal elasticity theory, *Latin American Journal of Solids and Structures*, Vol. 11, pp. 1541-1546, 2014.
- [12] M. Baghani, M. Mohammadi, A. Farajpour, Dynamic and stability analysis of the rotating nanobeam in a nonuniform magnetic field considering the surface energy, *International Journal of Applied Mechanics*, Vol. 8, No. 04, pp. 1650048, 2016.
- [13] M. Danesh, A. Farajpour, M. Mohammadi, Axial vibration analysis of a tapered nanorod based on nonlocal elasticity theory and differential quadrature method, *Mechanics Research Communications*, Vol. 39, No. 1, pp. 23-27, 2012.
- [14] A. Farajpour, M. Danesh, M. Mohammadi, Buckling analysis of variable thickness nanoplates using nonlocal continuum mechanics, *Physica E: Low-dimensional Systems and Nanostructures*, Vol. 44, No. 3, pp. 719-727, 2011.
- [15] A. Farajpour, M. R. Hairi Yazdi, A. Rastgoo, M. Loghmani, M. Mohammadi, Nonlocal nonlinear plate model for large amplitude vibration of magneto-electro-elastic nanoplates, *Composite Structures*, Vol. 140, pp. 323-336, 2016/04/15/, 2016.
- [16] A. Farajpour, M. Mohammadi, A. R. Shahidi, M. Mahzoon, Axisymmetric buckling of the circular graphene sheets with the nonlocal continuum plate model, *Physica E: Low-dimensional Systems and Nanostructures*, Vol. 43, No. 10, pp. 1820-1825, 2011/08/01/, 2011.
- [17] A. Farajpour, A. Rastgoo, M. Mohammadi, Surface effects on the mechanical characteristics of microtubule networks in living cells, *Mechanics Research Communications*, Vol. 57, pp. 18-26, 2014/04/01/, 2014.
- [18] A. Farajpour, A. Rastgoo, M. Mohammadi, Vibration, buckling and smart control of microtubules using piezoelectric nanoshells under electric voltage in thermal environment, *Physica B: Condensed Matter*, Vol. 509, pp. 100-114, 2017/03/15/, 2017.
- [19] A. Farajpour, A. R. Shahidi, M. Mohammadi, M. Mahzoon, Buckling of orthotropic micro/nanoscale plates under linearly varying in-plane load via nonlocal continuum mechanics, *Composite Structures*, Vol. 94, No. 5, pp. 1605-1615, 2012/04/01/, 2012.
- [20] A. Farajpour, M. Yazdi, A. Rastgoo, M. Mohammadi, A higher-order nonlocal strain gradient plate model for buckling of orthotropic nanoplates in thermal environment, *Acta Mechanica*, Vol. 227, No. 7, pp. 1849-1867, 2016.
- [21] M. R. Farajpour, A. Rastgoo, A. Farajpour, M. Mohammadi, Vibration of piezoelectric nanofilm-based electromechanical sensors via higher-order non-local strain gradient theory, *Micro & Nano Letters*, Vol. 11, No. 6, pp. 302-307, 2016.
- [22] N. Ghayour, A. Sedaghat, M. Mohammadi, Wave propagation approach to fluid filled submerged visco-elastic finite cylindrical shells, 2011.
- [23] M. Goodarzi, M. Mohammadi, A. Farajpour, M. Khooran, Investigation of the effect of pre-stressed on vibration frequency of rectangular nanoplate based on a visco-Pasternak foundation, 2014.

- [24] M. Mohammadi, A. Farajpour, M. Goodarzi, F. Dinari, Thermo-mechanical vibration analysis of annular and circular graphene sheet embedded in an elastic medium, *Latin American Journal of Solids and Structures*, Vol. 11, pp. 659-682, 2014.
- [25] M. Mohammadi, A. Farajpour, M. Goodarzi, R. Heydarshenas, Levy Type Solution for Nonlocal Thermo-Mechanical Vibration of Orthotropic Mono-Layer Graphene Sheet Embedded in an Elastic Medium, *Journal of Solid Mechanics*, Vol. 5, No. 2, pp. 116-132, 2013.
- [26] M. Mohammadi, A. Farajpour, M. Goodarzi, H. Mohammadi, Temperature Effect on Vibration Analysis of Annular Graphene Sheet Embedded on Visco-Pasternak Foundati, *Journal of Solid Mechanics*, Vol. 5, No. 3, pp. 305-323, 2013.
- [27] M. Mohammadi, A. Farajpour, M. Goodarzi, Numerical study of the effect of shear in-plane load on the vibration analysis of graphene sheet embedded in an elastic medium, *Computational Materials Science*, Vol. 82, pp. 510-520, 2014.
- [28] M. Mohammadi, A. Farajpour, A. Moradi, M. Ghayour, Shear buckling of orthotropic rectangular graphene sheet embedded in an elastic medium in thermal environment, *Composites Part B: Engineering*, Vol. 56, pp. 629-637, 2014.
- [29] M. Mohammadi, M. Ghayour, A. Farajpour, Free transverse vibration analysis of circular and annular graphene sheets with various boundary conditions using the nonlocal continuum plate model, *Composites Part B: Engineering*, Vol. 45, No. 1, pp. 32-42, 2013.
- [30] M. Mohammadi, M. Ghayour, A. Farajpour, Analysis of free vibration sector plate based on elastic medium by using new version of differential quadrature method, *Journal of Simulation and Analysis of Novel Technologies in Mechanical Engineering*, Vol. 3, No. 2, pp. 47-56, 2010.
- [31] M. Mohammadi, M. Goodarzi, M. Ghayour, S. Alivand, Small scale effect on the vibration of orthotropic plates embedded in an elastic medium and under biaxial in-plane pre-load via nonlocal elasticity theory, 2012.
- [32] M. Mohammadi, M. Goodarzi, M. Ghayour, A. Farajpour, Influence of in-plane pre-load on the vibration frequency of circular graphene sheet via nonlocal continuum theory, *Composites Part B: Engineering*, Vol. 51, pp. 121-129, 2013.
- [33] M. Mohammadi, M. Hosseini, M. Shishesaz, A. Hadi, A. Rastgoo, Primary and secondary resonance analysis of porous functionally graded nanobeam resting on a nonlinear foundation subjected to mechanical and electrical loads, *European Journal of Mechanics-A/Solids*, Vol. 77, pp. 103793, 2019.
- [34] M. Mohammadi, A. Moradi, M. Ghayour, A. Farajpour, Exact solution for thermo-mechanical vibration of orthotropic mono-layer graphene sheet embedded in an elastic medium, *Latin American Journal of Solids and Structures*, Vol. 11, pp. 437-458, 2014.
- [35] M. Mohammadi, A. Rastgoo, Nonlinear vibration analysis of the viscoelastic composite nanoplate with three directionally imperfect porous FG core, *Structural Engineering and Mechanics, An Int'l Journal*, Vol. 69, No. 2, pp. 131-143, 2019.
- [36] M. Mohammadi, A. Rastgoo, Primary and secondary resonance analysis of FG/lipid nanoplate with considering porosity distribution based on a nonlinear elastic medium, *Mechanics of Advanced Materials and Structures*, Vol. 27, No. 20, pp. 1709-1730, 2020/10/15, 2020.
- [37] M. Mohammadi, M. Safarabadi, A. Rastgoo, A. Farajpour, Hygro-mechanical vibration analysis of a rotating viscoelastic nanobeam embedded in a visco-Pasternak elastic medium and in a nonlinear thermal environment, *Acta Mechanica*, Vol. 227, No. 8, pp. 2207-2232, 2016.
- [38] H. Moosavi, M. Mohammadi, A. Farajpour, S. Shahidi, Vibration analysis of nanorings using nonlocal continuum mechanics and shear deformable ring theory, *Physica E: Low-dimensional Systems and Nanostructures*, Vol. 44, No. 1, pp. 135-140, 2011.
- [39] M. Safarabadi, M. Mohammadi, A. Farajpour, M. Goodarzi, Effect of surface energy on the vibration analysis of rotating nanobeam, 2015.
- [40] M. Mohammadi, A. Farajpour, A. Moradi, M. Hosseini, Vibration analysis of the rotating multilayer piezoelectric Timoshenko nanobeam, *Engineering Analysis with Boundary Elements*, Vol. 145, pp. 117-131, 2022/12/01/, 2022.
- [41] B. E. Launder, D. B. Spalding, *The numerical computation of turbulent flows*, in: *Numerical prediction of flow, heat transfer, turbulence and combustion*, Eds., pp. 96-116: Elsevier, 1983.
- [42] S. Azad, A. Riasi, H. Mahmoodi Darian, H. Amiri Moghadam, Parametric study of a viscoelastic RANS turbulence model in the fully developed channel flow, *Journal of Computational Applied Mechanics*, Vol. 48, No. 1, pp. 65-74, 2017.
- [43] T. Cebeci, P. Bradshaw, *Momentum transfer in boundary layers*, Washington, 1977.
- [44] J. Nikuradse, *Laws of flow in rough pipes*, 1950.

- [45] K. Choudhary, A. K. Jha, L. N. Mishra, M. Vandana, Buoyancy and chemical reaction effects on mhd free convective slip flow of newtonian and polar fluid through porousmedium in the presence of thermal radiation and ohmic heating with dufour effect, *Facta Universitatis. Series: Mathematics and Informatics*, Vol. 33, No. 1, pp. 001-029, 2018.
- [46] M. Choudhury, G. C. Hazarika, The effects of variable viscosity and thermal conductivity on mhd flow due to a point sink, *Matemáticas: Enseñanza Universitaria*, Vol. 16, No. 2, pp. 21-28, 2008.
- [47] P. Richards, R. Hoxey, Appropriate boundary conditions for computational wind engineering models using the k- $\epsilon$  turbulence model, *Journal of wind engineering and industrial aerodynamics*, Vol. 46, pp. 145-153, 1993.
- [48] B. Blocken, T. Stathopoulos, J. Carmeliet, CFD simulation of the atmospheric boundary layer: wall function problems, *Atmospheric environment*, Vol. 41, No. 2, pp. 238-252, 2007.
- [49] J. Franke, A. Hellsten, K. Schlünzen, B. Carissimo, Best practice guideline for the CFD simulation of flows in the urban environment-a summary, in *Proceeding of*, Cambridge Environmental Research Consultants, pp.
- [50] D. Hargreaves, N. G. Wright, On the use of the k- $\epsilon$  model in commercial CFD software to model the neutral atmospheric boundary layer, *Journal of wind engineering and industrial aerodynamics*, Vol. 95, No. 5, pp. 355-369, 2007.
- [51] Y. Yang, M. Gu, S. Chen, X. Jin, New inflow boundary conditions for modelling the neutral equilibrium atmospheric boundary layer in computational wind engineering, *Journal of Wind Engineering and Industrial Aerodynamics*, Vol. 97, No. 2, pp. 88-95, 2009.
- [52] C. v. Gortlé, J. Van Beeck, P. Rambaud, G. Van Tendeloo, CFD modelling of small particle dispersion: the influence of the turbulence kinetic energy in the atmospheric boundary layer, *Atmospheric environment*, Vol. 43, No. 3, pp. 673-681, 2009.
- [53] A. Parente, C. Gortlé, J. van Beeck, C. Benocci, A comprehensive modelling approach for the neutral atmospheric boundary layer: consistent inflow conditions, wall function and turbulence model, *Boundary-layer meteorology*, Vol. 140, No. 3, pp. 411-428, 2011.
- [54] M. Balogh, A. Parente, Realistic boundary conditions for the simulation of atmospheric boundary layer flows using an improved k- $\epsilon$  model, *Journal of wind engineering and industrial aerodynamics*, Vol. 144, pp. 183-190, 2015.
- [55] P. Richards, S. Norris, Appropriate boundary conditions for a pressure driven boundary layer, *Journal of Wind Engineering and Industrial Aerodynamics*, Vol. 142, pp. 43-52, 2015.
- [56] P. J. Richards, S. E. Norris, Appropriate boundary conditions for computational wind engineering: Still an issue after 25 years, *Journal of Wind Engineering and Industrial Aerodynamics*, Vol. 190, pp. 245-255, 2019.
- [57] C. Greenshields, The OpenFOAM foundation user guide 7.0, *The OpenFOAM Foundation Ltd: London, United Kingdom*, 10th July, 2019.
- [58] R. Lakshman, R. Basak, Analysis of transformed fifth order polynomial curve for the contraction of wind tunnel by using OpenFOAM, in *Proceeding of*, IOP Publishing, pp. 012048.
- [59] R. Lakshman, R. Basak, *Analysis of transformed sixth-order polynomial for the contraction wall profile by using OpenFOAM*, in: *Recent advances in theoretical, applied, computational and experimental mechanics*, Eds., pp. 133-144: Springer, 2020.
- [60] R. Lakshman, N. Pal, R. Basak, Comparative Analysis of Inlet Boundary Conditions for Atmospheric Boundary Layer Simulation Using OpenFOAM, in *Proceeding of*, Springer, pp. 79-86.
- [61] I. Abohela, On the Horizontal Homogeneity of the Atmospheric Boundary Layer Profile in CFD Simulations, *Appl. Math*, Vol. 12, No. 4, pp. 825-829, 2018.
- [62] L. H. Khurshudyan, W. H. Snyder, I. V. Nekrasov, Flow and dispersion of pollutants over two-dimensional hills, *Environment Protection Agency Report no EPA-600/4-81-067. Research Triangle Park*, 1981.